Check for updates

Sporadic absorption tomography using a conical shell X-ray beam

F. ELARNAUT,[1] J. P. O. EVANS,[1,*] D. DOWNES,[1] A. J. DICKEN,[1] S. X. GODBER,[2] AND K. D. ROGERS[3]

[1]*Imaging Science Group, Rosalind Franklin Building, Clifton, Nottingham Trent University, Nottingham, UK*
[2]*Halo X-ray Technologies, BioCity, Nottingham, UK*
[3]*Cranfield Forensic Institute, Cranfield University, Shrivenham, Swindon, UK*
*paul.evans@ntu.ac.uk

Abstract: We demonstrate tomography by measuring a sporadic sequence of ring shaped projections collected during a translational scan. We show that projections using 10% sampling may be used to construct optical sections with peak signal-to-noise ratio (PSNR) and structural similarity index (SSIM) of the order of 40 dB and 0.9, respectively. This relatively small degradation in image fidelity was achieved for a 90% potential reduction in X-ray dose coupled with a reduction in scan time. Our approach is scalable in both X-ray energy and inspection volume. A driver for our method is to complement previously reported conical shell beam techniques concerning the measurement of diffracted flux for structural analysis. This work is of great relevance to time critical analytical scanning applications in security screening, process control and diagnostic imaging.

References and links

1. F. Adams, "X-ray absorption and diffraction: overview," in *Encyclopedia of Analytical Science* (Elsevier, 2005), pp. 365–377.
2. S. Baumrind, F. H. Moffitt, and S. Curry, "The geometry of three-dimensional measurement from paired coplanar X-ray images," Am. J. Orthod. **84**(4), 313–322 (1983).
3. G. Chen, "Understanding X-ray cargo imaging," in *Nuclear Instruments and Methods in Physics Research, Section B: Beam Interactions with Materials and Atoms* (2005), pp. 810–815.
4. M. E. Coles, "8. X-Ray Imaging," in *Experimental Methods in the Physical Sciences* (1999), pp. 301–336.
5. A. Dicken, K. Rogers, P. Evans, J. Rogers, and J. W. Chan, "The separation of X-ray diffraction patterns for threat detection," Appl. Radiat. Isot. **68**(3), 439–443 (2010).
6. J. P. O. Evans, Y. Liu, J. W. Chan, and D. Downes, "View synthesis for depth from motion 3D X-ray imaging," Pattern Recognit. Lett. **27**(15), 1863–1873 (2006).
7. J. P. O. Evans and H. W. Hon, "Dynamic stereoscopic X-ray imaging," NDT Int. **35**(5), 337–345 (2002).
8. J. P. O. Evans and M. Robinson, "Design of a stereoscopic X-ray imaging system using a single X-ray source," NDT Int. **33**(5), 325–332 (2000).
9. A. J. Dicken, J. P. O. Evans, K. D. Rogers, N. Stone, C. Greenwood, S. X. Godber, J. G. Clement, I. D. Lyburn, R. M. Martin, and P. Zioupos, "Classification of fracture and non-fracture groups by analysis of coherent X-ray scatter," Sci. Rep. **6**(1), 29011 (2016).
10. F. Xu, L. Helfen, T. Baumbach, and H. Suhonen, "Comparison of image quality in computed laminography and tomography," Opt. Express **20**(2), 794–806 (2012).
11. P. Kandlakunta, R. Pham, R. Khan, and T. Zhang, "Development of multi-pixel x-ray source using oxide-coated cathodes," Phys. Med. Biol. **62**(13), N320–N336 (2017).
12. M. Hassan, J. A. Greenberg, I. Odinaka, and D. J. Brady, "Snapshot fan beam coded aperture coherent scatter tomography," Opt. Express **24**(16), 18277–18289 (2016).
13. C. K. Egan, S. D. M. Jacques, M. D. Wilson, M. C. Veale, P. Seller, A. M. Beale, R. A. D. Pattrick, P. J. Withers, and R. J. Cernik, "3D chemical imaging in the laboratory by hyperspectral X-ray computed tomography," Sci. Rep. **5**(1), 15979 (2015).
14. S. Singh and M. Singh, "Explosives detection systems (EDS) for aviation security," Signal Proc. **83**(1), 31–55 (2003).
15. K. Wells and D. A. Bradley, "A review of X-ray explosives detection techniques for checked baggage," Appl. Radiat. Isot. **70**(8), 1729–1746 (2012).
16. G. Harding, "X-ray diffraction imaging-A multi-generational perspective," Appl. Radiat. Isot. **67**(2), 287–295

(2009).

17. A. Dicken, K. Rogers, P. Evans, J. W. Chan, J. Rogers, and S. Godber, "Combined X-ray diffraction and kinetic depth effect imaging," Opt. Express **19**(7), 6406–6413 (2011).

18. D. J. Brady, *Optical Imaging and Spectroscopy*, 1st ed. (Wiley, 2009).

19. A. P. Cuadros and G. R. Arce, "Coded aperture optimization in compressive X-ray tomography: a gradient descent approach," Opt. Express **25**(20), 23833–23849 (2017).

20. A. P. Cuadros, C. Peitsch, H. Arguello, and G. R. Arce, "Coded aperture optimization for compressive X-ray tomosynthesis," Opt. Express **23**(25), 32788–32802 (2015).

21. Y. Kaganovsky, D. Li, A. Holmgren, H. Jeon, K. P. MacCabe, D. G. Politte, J. A. O'Sullivan, L. Carin, and D. J. Brady, "Compressed sampling strategies for tomography," J. Opt. Soc. Am. A **31**(7), 1369–1394 (2014).

22. P. Evans, K. Rogers, J. Chan, J. Rogers, and A. Dicken, "High intensity X-ray diffraction in transmission mode employing an analog of Poisson's spot," Appl. Phys. Lett. **97**(20), 204101 (2010).

23. A. Dicken, A. Shevchuk, K. Rogers, S. Godber, and P. Evans, "High energy transmission annular beam X-ray diffraction," Opt. Express **23**(5), 6304–6312 (2015).

24. P. Evans, K. Rogers, A. Dicken, S. Godber, and D. Prokopiou, "X-ray diffraction tomography employing an annular beam," Opt. Express **22**(10), 11930–11944 (2014).

25. A. J. Dicken, J. P. O. Evans, K. D. Rogers, C. Greenwood, S. X. Godber, D. Prokopiou, N. Stone, J. G. Clement, I. Lyburn, R. M. Martin, and P. Zioupos, "Energy-dispersive X-ray diffraction using an annular beam," Opt. Express **23**(10), 13443–13454 (2015).

26. D. Prokopiou, K. Rogers, P. Evans, S. Godber, and A. Dicken, "Discrimination of liquids by a focal construct X-ray diffraction geometry," Appl. Radiat. Isot. **77**, 160–165 (2013).

27. F. Li, Z. Liu, and T. Sun, "Annular beam high-intensity X-ray diffraction based on an ellipsoidal single-bounce monocapillary," J. Appl. Cryst. **49**(2), 627–631 (2016).

28. J. P. O. Evans, S. X. Godber, F. Elarnaut, D. Downes, A. J. Dicken, and K. D. Rogers, "X-ray absorption tomography employing a conical shell beam," Opt. Express **24**(25), 29048–29059 (2016).

29. Nikon Metrology Inc, "XT V 160 Electronics X-ray inspection system," https://www.nikonmetrology.com/en-gb/product/xt-v-160.

30. Microsoft Inc, "rand," https://msdn.microsoft.com/en-us/library/398ax69y.aspx.

31. P. Mohammadi, A. Ebrahimi-Moghadam, and S. Shirani, "Subjective and Objective Quality Assessment of Image," Survey (Lond.) **41**, 6738079 (2014).

32. A. M. Beale, S. D. M. Jacques, E. K. Gibson, and M. Di Michiel, "Progress towards five dimensional diffraction imaging of functional materials under process conditions," Coord. Chem. Rev. **277–278**, 208–223 (2014).

33. J. Dörr, M. Rosenbaum, W. Sauer-Greff, and R. Urbansky, "Automatic focus algorithms for TDI X-Ray image reconstruction," Adv. Radio Sci **10**, 145–151 (2012).

1. Introduction

Rapid non-destructive characterization of extended (mm sized) objects is an essential requirement for material science [1–3], security screening [4–8] and medicine [9]. At the mm length scale non-destructive structural probes are limited mostly to highly penetrating radiation, such as hard X-ray. Volumetric X-ray imaging techniques such as CT (computerized tomography), X-ray tomosynthesis [7], laminography [10] and phase contrast imaging [3] have developed into rapid screening tools where mass attenuation coefficients and refractive indices provide the contrast mechanisms, respectively. In addition recent advances in switched X-ray sources [11] demonstrate the potential to replace mechanical scanning.

Many applications would benefit from material phase identification or structural information attributed to components distributed within an inspection volume. For example, coded aperture coherent scatter tomography [12] and hyperspectral X-ray computed tomography [13] show great promise but significant challenges remain in dealing with a jumble of complex objects encountered routinely in real-world applications. Our work is primarily aimed at the security screening of air passenger luggage, which routinely employs X-ray absorption imaging to help detect shape-based threats such as guns, knives and sharps. However, highly shape-variant threats including narcotics and a wide range of plastic, liquid and homemade explosives (HMEs) require material specific information for enhanced false-alarm resolution [14–16]. We have previously reported; see Section 2.1, the benefits of materials characterization employing X-ray diffraction (XRD) tomography along with other conical shell or annular beam techniques. It follows that if high-energy X-ray absorption and diffraction probe [16,17] were successfully combined via a cost-effective technology, then it could be deployed to increase the throughput of carry-on and checked luggage at international

airports and other travel hubs. This development would be a major and disruptive advance for security screening applications.

To augment our earlier work we report a study of tomography employing the sporadic collection of conical shell projections or *focal construct geometry* (FCG). We demonstrate our technique by scanning phantoms through the beam. While each shell projection is sampled fully via an X-ray image intensifier the collection points are pseudorandomly distributed throughout the translational scan. Pixels composing the sporadically scanned object are composited to produce a series of partially sampled oblique projections. In this work we have adopted the term sporadic sampling to differentiate our approach from compressed or sparse sensing involving solutions to underdetermined linear systems [18–20]. Specifically we do not make assumptions concerning the 'sparsity' or degree of 'compressibility' [21] of our non-sporadically (100%) sampled data. Instead, we apply a deterministic algorithm to construct optical sections. Such an approach does not require the setting of convergence criteria inherent in iterative methods. In our case the construction of optical sections requires a sequence of normalization maps to be synthesized to enable the proper weighting of the variable contributions from relatively small data acquisitions. The application of such tomosynthesis employing sporadically sampled projections is very promising as it potentially reduces X-ray dose and scanning time by significant amounts dependent upon the physical implementation of the X-ray scanning process e.g. single source or multiple sources/emitters. It also dovetails into the ongoing development of a combined XRD and absorption FCG technique employing a single X-ray beam and sensor.

Our paper is organised as follows. Section 2 presents the methods including the theory background, our new imaging technique and describes the experiment conditions. Section 3 presents our experiment results and discussion. Section 4 summarizes our conclusions and the implications of our findings and the future direction of the work.

2. Methods

2.1 Theory background

Focal construct geometry (FCG) refers to an alternate X-ray beam topology designed to reduce the exposure time required for the collection and analysis of coherent scatter from samples. This approach employs a conical shell X-ray beam to provide extended gauge volumes, which produce relatively high intensity focal spots [22,23] and caustics in the diffracted flux [24]. The FCG method has been applied in energy dispersive [25] and angular dispersive modes [24,26,27], used to identify liquid samples [26], and shown to deal favorably with non-ideal samples in which scattering distributions are adversely affected by large grain size and crystallographic textures [27]. Scanning techniques employing FCG include angular-dispersive X-ray diffraction tomography [24] and absorption contrast tomography [28]. This paper reports a complementary and novel tomographic method employing sporadically distributed conical shell projections.

2.2 New imaging method

Our imaging method collects a series of conical shell projections during a two axis translational scan of an object through a conical shell beam of X-rays. The perspective center of each projection is identified on a rectilinear sampling grid, which in practice corresponds to the relative (x, y) coordinate position of the point source, see Fig. 1 (right). The source and detector form a rigid body during the scan with each undergoing a relative to object in-plane translation. In this work a subset of sporadically distributed grid positions or nodes are employed to collect projections. The chosen node positions follow a pseudorandom pattern, which is represented as a binary image or map ρ where the pixel centers correspond to the node positions, see Fig. 1 (left). The map has the dimensions in pixels (x_ρ, y_ρ) and image acquisitions are represented by unity and unused positions are represented by zero. The

scanned area enclosed by the grid is $A = S^2 x_\rho y_\rho$, where S is the axial step distance between neighboring acquisition points.
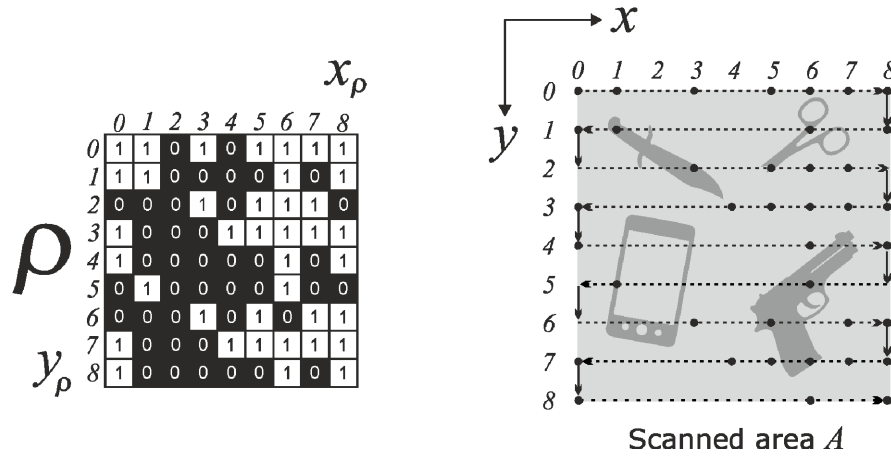

Fig. 1. Binary image or map ρ representing the pseudorandom distribution of (annular) image acquisition points with unity pixels and non-acquisitions or nulls with zero pixels. A rectilinear sampling grid of X-ray source positions over the scanned area A is related to ρ by scaling the separation between pixel centers by the scan step size S.

For each sampling position on the rectilinear sampling grid, the axial distances to absorption X-ray measurements made with a sensor element $I(l, \gamma)$ are given by

$$x = Sx_\rho + l \cos \gamma \tag{1}$$

$$y = Sy_\rho + l \sin \gamma \tag{2}$$

where l is the physical radius of the annular sensor and γ is the angular distance. Thus, absorption measurements taken from specific circumferential (l, γ) sensor elements can provide a pixel stream that may be composited to form sporadically sampled sets of oblique projections along a fixed direction γ as illustrated in Fig. 2.
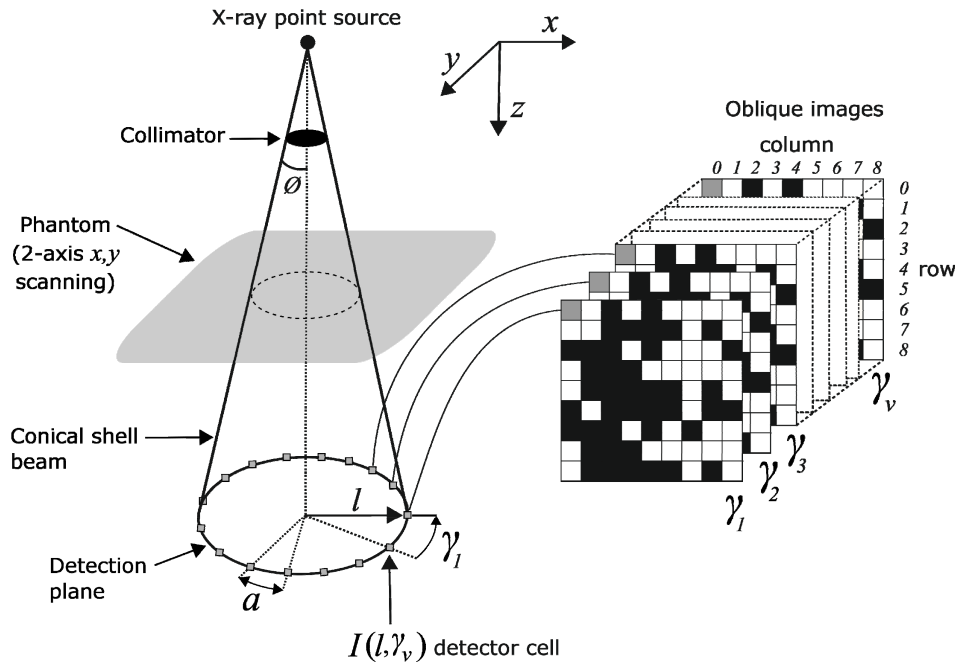
Fig. 2. Pixels recorded at fixed circumferential locations from each conical shell X-ray projection are composited to form a sporadically sampled oblique projection. The total number of projections are limited by the resolution of the annular sensor (or virtual equivalent). The resolution in pixels of each oblique image equates to the total number of potential acquisition points in the full sampling grid. The relative position of pixels representing nulls (highlighted in black) is identical for every oblique projection as defined by the map ρ.

We obtain a sequence of different, equally sporadically sampled, oblique projections M, where each digital image $M(\gamma)$ has dimensions in pixels. The angular separation a between neighboring oblique views is then given by

$$a = \frac{2\pi}{v}.$$

(3)

Where v, the total number of circumferential sampling positions also determines the total number of oblique projections that may be composited. To recover optical sections over successive focal plane positions requires an appropriate shift algorithm. To effect a focal plane each oblique image composing the sequence M should be shifted a constant linear distance r along their respective projection directions γ, see Fig. 3. Image centers (x_M, y_M) in sequence M are shifted to effect a new relative registration (x_D, y_D) in the new image sequence D.

For each pixel $D(\gamma, x_D, y_D)$ in image $D(\gamma)$ of image sequence D

$$D(\gamma, x_D, y_D) = M(\gamma, x_M, y_M)$$

(4)

where

$$x_D = \lfloor x_M + r\cos\gamma + 0.5 \rfloor$$
$$y_D = \lfloor y_M + r\sin\gamma + 0.5 \rfloor$$
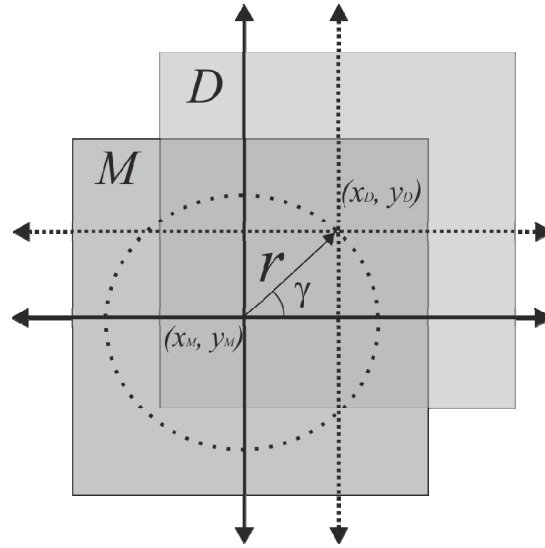
(5)

and r is a constant.

Fig. 3. An example radial shift applied to image set M to form a reregistered sequence of oblique images D.

To extract normalized optical sections requires that the total number of "in focus pixel" contributions be mapped over the full range of focal plane positions to discount "null pixels" in the tomosynthesis. To facilitate this process a contribution or normalization map ω is generated for each focal plane using the following:

$$\omega = \sum_{i=1}^{v} D_\rho (i) \tag{6}$$

where D_ρ is obtained from Eq. (4) with substitution of the image sequence M with a sequence of (identical) maps ρ, termed M_ρ. Thus given $r = n\delta r$ and δr is the minimum radial shift increment and $n = 0,1,2,....,N.$ a full set of contribution maps ω may be synthesized from Eq. (6) over the range N by varying the constant r in Eq. (5). For example, the inspection volume is bounded by two hypothetical focal planes. The near bound is coincident with the point source $r = 0,$ while the far bound is coincident with the detection plane $r = N\delta r.$ Through similar considerations and by applying Eqs. (4)-(6) a set of summed sporadically sampled oblique projections G for given r are given by

$$G = \sum_{i=1}^{v} D(i). \tag{7}$$

The associated ω contribution map may then be applied for each focal plane position to construct a normalized optical section R

$$R(x,y) = \frac{G(x,y)}{\omega(x,y)}. \tag{8}$$

Where R is a digital optical section for a given focal plane position with shift r.

2.3 Experiment setup

A commercial X-tek VTX160 X-ray system was used to collect all the X-ray measurements presented in this work. The detailed specifications of the system can be found on the Nikon Metrology website [29]. This instrument is housed in a cabinet and originally intended for

real-time inspection of printed circuit boards and the like. It has a micro focus X-ray generator and a three-axis motion stage. Conical shell projections were collected from a ring shaped ROI on a Hamamatsu V8926P image intensifier with a CsI phosphor input screen. The intensifier is optically coupled to an AVT Manta G-145 GigE camera capturing 1280x1024x8 bit images. A complete set of conical shell projections were collected according to a rectilinear sampling grid. This data set was used to construct the ground truth optical sections used for comparative analysis.

The map ρ is a digital binary image parameterized according to the chosen scan dimensions and sampling level. Pseudorandom integers generated by the C + + library function *rand()* [30] provide unique ordered pairs to form sampling coordinates. The map informs the sporadic scan via scaling by the scan step size S. The digital map is also processed to establish the contribution or normalization maps ω within the tomosynthesis.

In this work the ground truth is defined as 100% sampling, which indicates that all positions in a sampling grid were used for sampling and optical section construction. The effect of different amounts of sampling upon the fidelity of the optical sections with respect to ground truth was measured using peak signal-to-noise ratio (PSNR) and structural similarity index (SSIM) [31]. In this study the signal component within the PSNR calculation is defined as the non-sporadic (100%) sampled reconstructed image [19]. SSIM and PSNR values were calculated at successive axial increments along the full theoretical range of the experiment system i.e. bounded by the point source and detector surface. In addition, a metric termed fill factor describes the ratio of constructed pixels derived from X-ray measurements to null pixels in a given optical section. This approach was found useful as it enables the effect of relative sampling amounts upon the constructed image parameters to be studied via a fill factor-radial shift characteristic.

Two different phantoms were fabricated and employed in our experiments. A calibrated phantom was constructed using acrylic sheets, see Fig. 4, with each layer supporting readily recognizable flat shapes, cut out from a sheet of tin, that resemble a mobile phone, knife, scissors and a gun. The relative axial scale of the shapes is roughly correct. The X-ray absorption contrast produced by the tin material provided the image forming signal for our experiments. This phantom was designed to establish proof-of-principle of our novel method and support the analysis of the reconstructed image parameters.
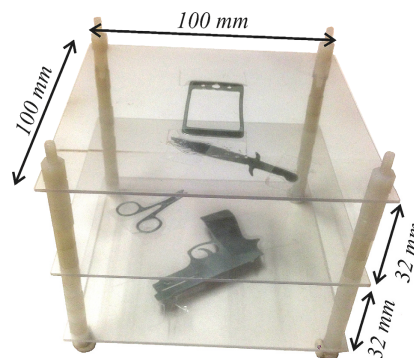

Fig. 4. Calibrated phantom (~1:4 scale) comprising of 100 mm square, 1 mm thick acrylic sheets supporting flat shapes fabricated from 0.15 mm thick tin. The "knife" and the "scissors" are both on the middle layer with the "phone" and the "gun" on the top and bottom layers, respectively.

The X-ray source accelerating voltage and current were set to $70 \, kV$ and $60 \, \mu A$, respectively. Conical shell projections with a half opening angle $\phi = 117.64 \, mradians$ were collected from a ring shaped ROI, $l = 48 \, mm$, on the image intensifier. The corresponding radius on the optically coupled camera was 500 pixels with an exposure time of $70 \, ms$. The

total period of time required to collect data from each rectilinear grid position equates to $100\,ms$. The separation between the input window of the intensifier and the point source was set at $406\,mm$ throughout the experiment. The phantom was raster scanned through 500 positions along the x and y axes in steps of $S = 280\,\mu m$ over a total scanned area of $140\text{x}140\,mm^2$.

A second phantom featuring objects with irregular and complex morphology was designed to be more representative of a "real life" application, see Fig. 5. The phantom comprises of an aggregate of objects to represent a core section through a luggage item to emulate a security screening scenario.
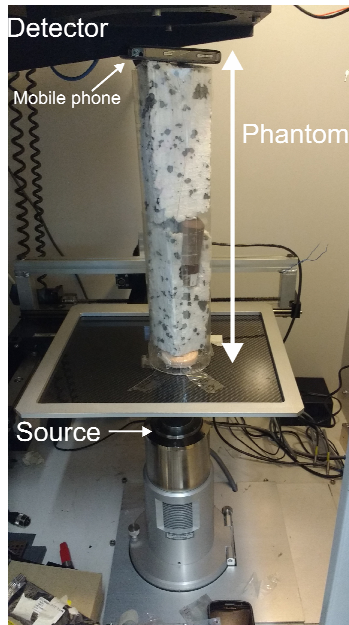

Fig. 5. Luggage core phantom mounted on the carbon fiber translation table in the X-ray inspection chamber. An aggregate of discrete objects, arranged along a ~40 cm component of the z-axis, were supported by polystyrene foam. A mobile phone was positioned nearest the image intensifier input window and a disc of soap together with a paperclip nearest the source. Midway along the core a plastic marker pen (elliptical cross-section) and a medical inhaler containing a pressurized canister (circular cross-section) were arranged with their long axes approximately parallel to the principal phantom axis. Also, two fine gauge wires run from a circular metal contact (initially as a twisted pair) at the center of the soap along the full length of the phantom to the phone.

The system setup was changed to accommodate the second phantom's physical dimensions. In this experiment the X-ray source accelerating voltage and current were set to $80\,kV$ and $70\,\mu A$, respectively. Conical shell projections with a half opening angle $\phi = 62.8\,mradians$ were collected from a ring shaped ROI, $l = 33.6\,mm$, on the image intensifier. The corresponding radius on the optically coupled camera was 350 pixels with an exposure time of $70\,ms$. The separation between the input window of the intensifier and the point X-ray source was set at $530\,mm$ throughout the experiment. The phantom was raster scanned through 700 positions along the x and y axes in steps of $S = 200\,\mu m$ over a total scanned area of $140\text{x}140\,mm^2$.

3. Results and Discussion

3.1 Pseudorandom maps

Pseudorandom data was generated as described in Section 2.3 and used to construct binary maps ρ with sampling levels of 50%, 20% and 10%, respectively, see Fig. 6. The maps were then used to inform data collection and produce optical sections from the calibrated phantom to support a comparative analysis of constructed image parameters.

Fig. 6. Examples showing (32x32) areas extracted from higher resolution (500x500) pseudorandom maps ρ of sampling levels; left (50%), middle (20%) and right (10%). The black pixels have a one-to-one relationship with nulls in the oblique projections.

To calculate the associated fill factors Eqs. (4)-(6) were applied to each (full resolution) map shown in Fig. 6 to produce a sequence of contribution maps ω. The resultant characteristic plotted in Fig. 7 shows the fill factor as a function of the radial shift r. This shift also enumerates a sequence of focal plane positions where the separation between neighboring planes is constant and independent of position.
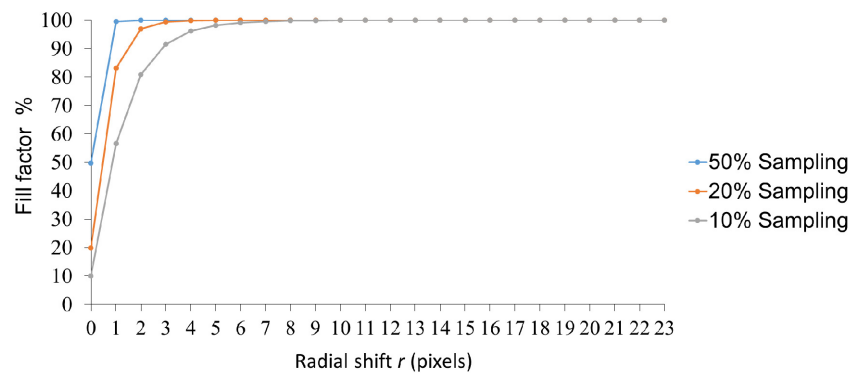

Fig. 7. Fill factor - radial shift characteristics for contribution or normalization maps ω (500x500 pixels) with sampling levels of 50%, 20% and 10%, respectively. The range of r is truncated to illustrate initial growth.

The minimum value at the intercept is given by the sampling level set by ρ at a zero radial shift value whereupon each map exhibits one-to-one registration and $\omega = \rho v$. The initial rate of change of fill factor increases with increasing sampling as expected. The shape of this characteristic is largely independent of pixel resolution as can be appreciated from 700x700 contribution maps shown in Fig. 8, which were calculated in preparation for imaging the "luggage phantom".
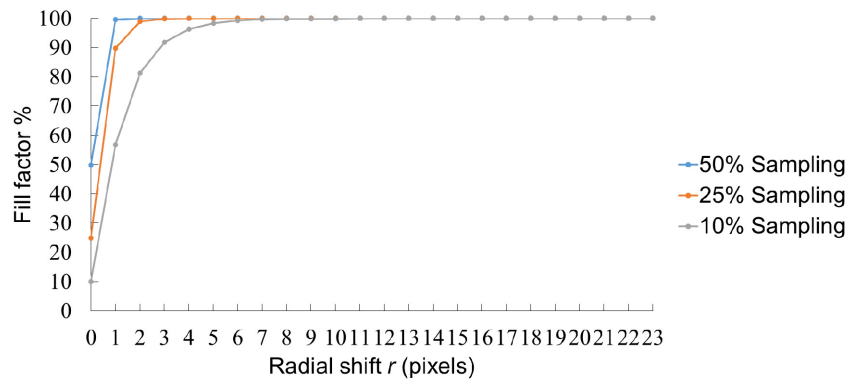
Fig. 8. Fill factor - radial shift characteristics for contribution or normalization maps ω (700x700 pixels) with sampling of 50%, 25% and 10%, respectively. The range of r is truncated to illustrate initial growth.

The following Section 3.2 presents the analysis of optical section fidelity as a function of the sampling level of the pseudorandom mapping process.

3.2 Sporadically sampled oblique images and tomosynthesis

The calibrated phantom was placed within the inspection volume and was raster scanned along the x-axis and the y-axis according to the experiment conditions described in Section 2.3. The full scan data provided the ground truth X-ray measurements for the comparative analysis of the reconstructed image parameters. The maps ρ described in Section 3.1 were applied to select subsets of this data to emulate different amounts of sporadic sampling. The physical coordinate positions of the measurements made with a sensor element $I(\gamma, l)$ are given by Eqs. (1) and (2). The angular separation between each successive oblique view $a \approx 1.75 \, mradians$ from Eq. (3). Shift-and-add tomosynthesis was applied following Eqs. (4)-(8) to produce a comparative series of optical sections R, examples of which are shown in Fig. 9 with supporting PSNR and SSIM values given in Table 1.
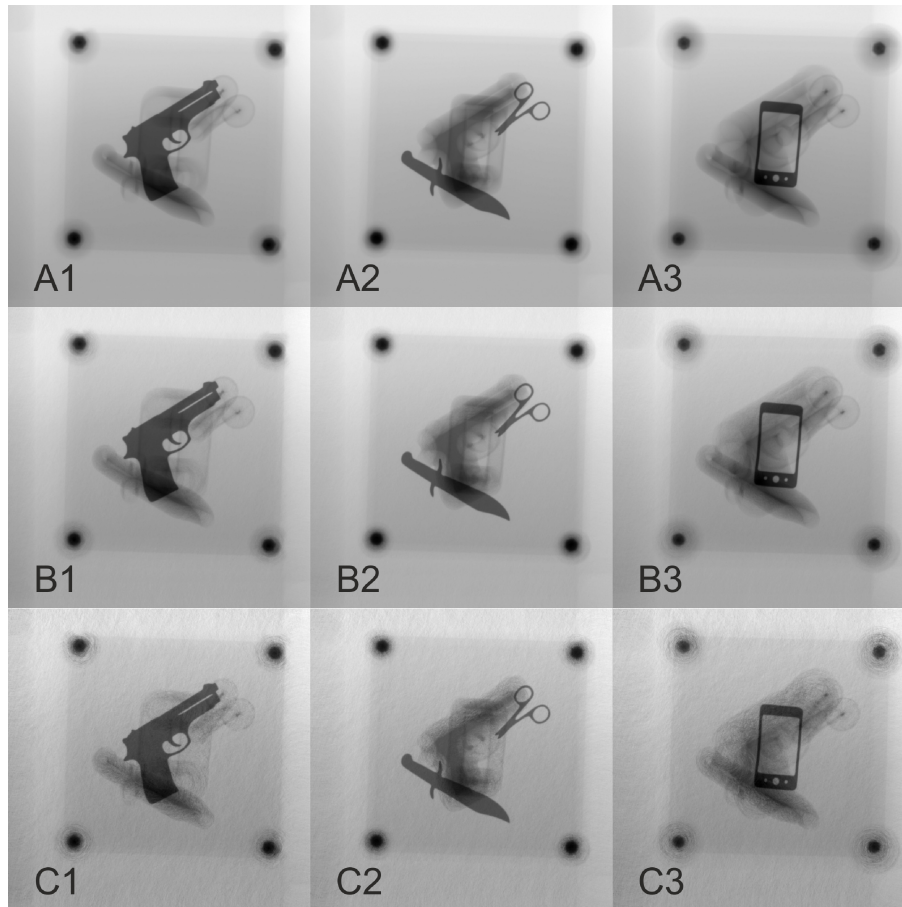
Fig. 9. Optical sections from the calibrated phantom. Row A is 100% sampling or Ground Truth, Row B 50% sampling, and Row C 10% sampling. Column 1 shows the layer *(z = 106 mm, r = 46 pixels)* nearest the source containing the gun shape, column 2 shows the middle layer *(z = 137 mm, r = 59 pixels)* containing the knife and scissors, and column 3 the layer nearest the detector *(z = 167 mm, r = 72 pixels)* containing the phone shape; where the preceding values *(z, r)* specify the focal plane position and the digital shift radius, respectively. All oblique images and optical sections have a resolution of 500x500 pixels. A direct comparison of optical sections at successive focal plane positions can be seen in (Visualization 1) for; 100%, 50%, 20% and 10% sampling, where a frame-by-frame readout of the corresponding PSNR and SSIM are provided within a video montage.
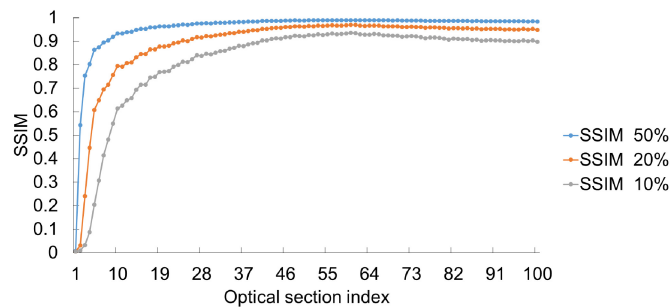

Fig. 10. SSIM of optical sections (500x500 pixels) from the calibrated phantom for 50%, 20% and 10% sampling.

Table 1. Calibrated phantom PSNR and SSIM for rows B and C indexed in Fig. 9 (where row A is Ground Truth). Row B′ provides additional values.

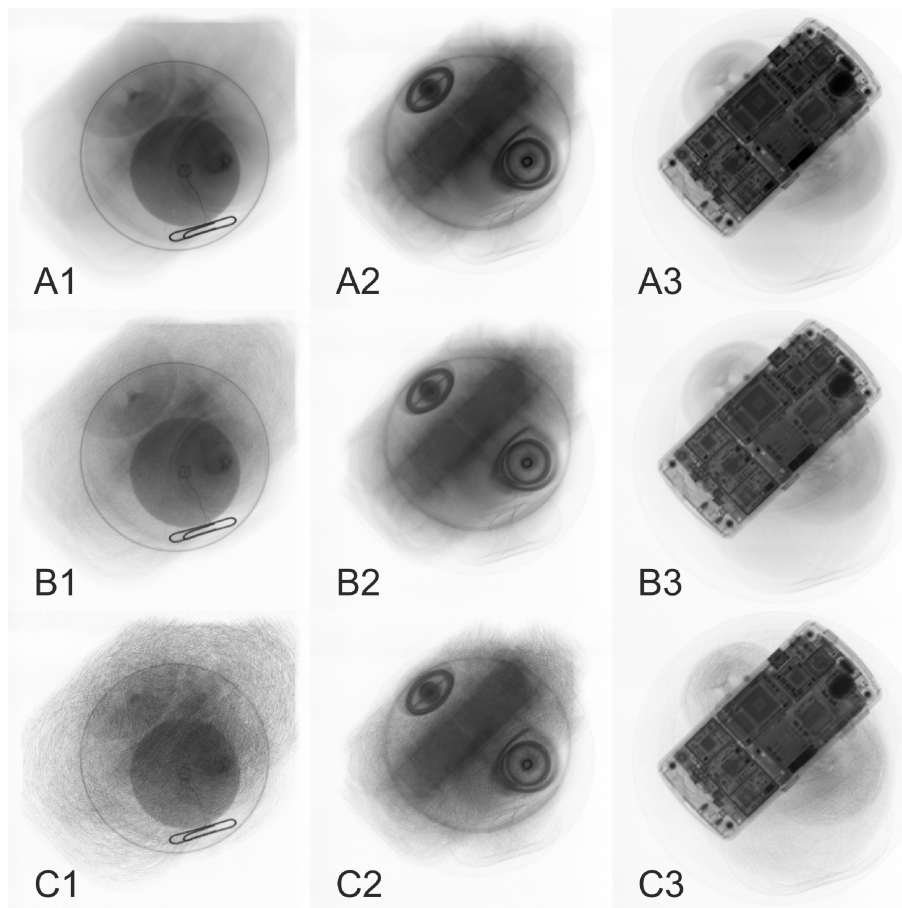|		1		2		3	
	Sampling (%)	PSNR (dB)	SSIM	PSNR (dB)	SSIM	PSNR (dB)	SSIM
B	50	48.4	0.988	49.1	0.990	48.5	0.988
B′	20	42.9	0.961	43.8	0.968	43.0	0.961
C	10	39.4	0.918	40.3	0.932	39.4	0.920

Fig. 11. Optical sections from the luggage phantom. Row A 100% sampling is Ground Truth, Row B 50% sampling, and Row C 10% sampling. Column 1 nearest the source *(z = 114mm, r = 36 pixels)* shows the disc of soap together with a paperclip, column 2 midway *(z = 292 mm, r = 92 pixels)* shows a plastic marker pen (elliptical cross-section) and a medical inhaler containing a pressurized canister (circular cross-section), and column 3 nearest the detector *(z = 502 mm, r = 158 pixels)* the mobile phone; where the preceding values *(z, r)* specify the focal plane position and the digital shift radius, respectively. All oblique images and optical sections have a resolution of 700x700 pixels. A direct comparison of optical sections at successive focal plane positions can be seen in (Visualization 2) for; 100%, 50%, 25% and 10% sampling, where a frame-by-frame readout of the corresponding PSNR and SSIM are provided within a video montage.

The plot of SSIM versus optical section shown Fig. 10 is consistent with the fill factor characteristic presented in Fig. 7. The near zero SSIM for the initial optical section was expected as the corresponding fill factor is at a minimum e.g. 10% sampling equates to 90% of constructed pixels being null (allocated a zero value). It can be appreciated that this

hypothetical axial position subtends the point source and therefore cannot be used to effect an in focus section. The high rate of change of the "pre-knee" fill factor corresponds to rapid improvement in SSIM. However, in practice the aforementioned limitations are superseded by the minimum inspection distances imposed by the physical system components e.g. beam shaping optics and or collimators.

In a second experiment the luggage phantom was placed within the inspection volume and was raster scanned along the x-axis and the y-axis in a similar fashion to the calibrated phantom previously described but this time with higher resolution 700x700 maps, as described in Section 2.3. Shift-and-add tomosynthesis was applied following Eqs. (4)-(8) to produce a comparative series of optical sections R, examples of which are shown in Fig. 11 with supporting PSNR and SSIM values provided in Table 2.

Table 2. Luggage phantom PSNR and SSIM for rows B and C indexed in Fig. 11 (where row A is Ground Truth). Row B′ provides additional values.

		1		2		3	
	Sampling (%)	PSNR (dB)	SSIM	PSNR (dB)	SSIM	PSNR (dB)	SSIM
B	50	37.9	0.899	44.6	0.975	47.5	0.987
B′	25	33.2	0.782	39.9	0.938	43.2	0.967
C	10	28.3	0.627	35.2	0.861	38.6	0.921

The plot of SSIM versus optical section shown in Fig. 12 is consistent with the fill factor characteristic presented in Fig. 8. However the knee of graph for the core phantom data is softer in comparison to that graphed for the calibrated phantom in Fig. 10.
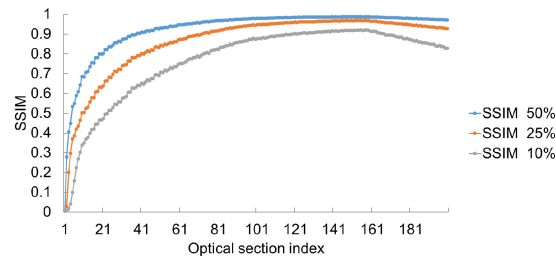

Fig. 12. SSIM of optical sections (700x700 pixels) from the luggage core phantom for 50%, 25% and 10% sampling.

This observation is attributed to the increased density and thickness of the aggregate of objects composing the luggage phantom. For example, an optical section through the low density disc of soap exhibits significantly increased artifacts in comparison to ground truth. It was observed that these artifacts arise primarily from the defocusing of the relatively high density mobile phone, which becomes less effective with decreasing sampling. The converse focusing situation results in a relatively high quality optical section of the mobile phone. These observations are consistent with the reduction in the total number of contributing pixels being input to the tomosynthesis, which is identified as the main limiting factor of the imaging fidelity of our method.

4. Conclusion

We have described in theory and verified experimentally novel sporadic sampling applied to absorption FCG tomosynthesis. Constructed images have been produced from relatively small data acquisitions. Sampling levels of 10% resulted in relatively little degradation in the constructed image parameters. The fidelity of the optical sections according to PSNR and SSIM measurements were of the order of 40 dB and 0.9, respectively. These findings support the hypothesis that the total number of X-ray measurements can be reduced by 90% in

comparison with our fully sampling or "ground truth method". It follows that a commensurate reduction in X-ray dose and reduced scanning times are possible. However, to calculate the exact amount would be dependent upon the physical parameters such as the duty cycle of the X-ray source or multiple X-ray emitters and the associated scanning or switching limitations. Nonetheless significant reductions are realistically anticipated.

Specifically, we demonstrate that a sporadic set of conical shell projections collected over a two axis translational scan can be composited to form a set of pseudorandom partially sampled oblique projections. The relative coordinate positions of nulls in each oblique image are parameterized by a digital representation of the sampling grid used to inform the scanning of objects under inspection. The application of tomosynthesis incorporating a sequence of normalization maps has been created and implemented to enable the proper weighting of the variable contributions from relatively small data acquisitions. Given this deterministic algorithmic approach we plan to apply compressive sensing and iterative methods [21] to seek further improvements in image fidelity, dose and data collection times. We also plan to compare and contrast the sporadic FCG method with other beam topologies inspired by compressive sensing. However, the advantages of FCG applied to the collection of diffracted flux are usually not present in competing absorption modalities.

Our work is a critical step towards combining XRD and absorption FCG via a common beam topology and supports the working hypothesis that real-time operational speeds can be achieved by employing multi-emitter sources. Our ultimate aim is to develop the technological basis for a novel compact and cost effective material specific 3D scanner. We believe that such an approach has many potential applications in security screening [14–16], process control [32,33] and diagnostic bone 'quality' imaging [9].

Funding